



Well-dispersed iron nanoparticles exposed within nitrogen-doped mesoporous carbon nanofibers by hydrogen-activation for oxygen-reduction reaction



Geon-Hyoung An, Eun-Hwan Lee, Hyo-Jin Ahn*

Department of Materials Science and Engineering, Seoul National University of Science and Technology, Seoul 139–743, South Korea

ARTICLE INFO

Article history:

Received 31 July 2015

Received in revised form

11 April 2016

Accepted 6 May 2016

Available online 8 May 2016

Keywords:

Oxygen-reduction reaction

Iron nanoparticles

Nitrogen-doped carbon nanofiber

High surface area

Mesoporous structure

ABSTRACT

Well-dispersed Fe nanoparticles exposed within N-doped mesoporous carbon nanofibers (Fe–NMCNF) are synthesized using electrospinning and H₂-activation. Their morphologies, crystal structures, chemical bonding states, and electrochemical performance are demonstrated at three calcination temperatures (700, 800, and 900 °C) during H₂-activation. Fe–NMCNF calcined at 800 °C had a high specific surface area of 467.6 m² g^{−1}, total pore volume of 0.88 cm³ g^{−1}, large average pore size of 7.5 nm, and large mesopore volume fraction of 79.1%. In particular, the Fe–NMCNF sample calcined at 800 °C exhibits both excellent catalytic activity for oxygen reduction reaction and superb long-term stability compared to commercial Pt/C in acid electrolyte of 0.1 M HClO₄. The performance improvement results from the combined effect of the well-dispersed Fe nanoparticles exposed within N-doped mesoporous CNFs and the uniform morphology of mesoporous CNFs.

© 2016 Elsevier B.V. All rights reserved.

1. Introduction

The development of an oxygen-reduction reaction (ORR) process in a cathode is a key technology for next-generation applications such as proton-exchange-membrane fuel cells (PEMFCs) and metal–air batteries [1–4]. Because it is more difficult for cathodic reactions like ORR to proceed and they are slower when compared to anodic reactions, the performance of these devices can be affected by the ORR process [5,6]. As reported, platinum (Pt) catalysts have been widely used in the ORR process because of their excellent electrocatalytic activity [7]. However, Pt catalysts suffer from critical disadvantages such as high cost, limited long-term stability, and large over-potential loss [8,9]. Therefore, much effort has been devoted to develop non-Pt catalysts with superb electrocatalytic activity [10]. Among previously reported non-Pt catalysts, the most promising candidate since the pioneering research of Jasinski in 1964 is the metal- and N-doped carbon (M–N–C; M = Fe, Co) [11]. These M–N–C catalysts have recently been reported as efficient ORR catalysts with both excellent catalytic activity and long-term stability [11–17]. Especially, N content is a very important factor for the improved electrochemical

performance in the ORR process because the N-doped carbon assisted O₂ adsorption and decomposition of intermediate hydroperoxide (HO₂[−]) to oxygen [13,14]. Using pyrolysis with melamine and a Fe-containing precursor, Peng et al. [18] synthesized Fe- and N-doped graphene, which exhibited good ORR activity in an acid electrolyte. Liu et al. [19] reported that Fe carbide nanoparticles embedded within N-doped porous carbon nanosheets exhibited good ORR activity in an acid electrolyte. Hu et al. [20] reported that hollow spheres of Fe₃C nanoparticles encased in graphitic layers showed high ORR activity and superb long-term stability in an acid electrolyte. Nevertheless, most of these materials showed poor catalytic activity in acid electrolytes when compared to commercial Pt-doped carbon (Pt/C) catalysts [21]. Thus, further improvements in the catalytic activity of M–N–C catalysts in acid electrolytes are highly desired.

In order to improve the ORR activity and long-term stability, carbon-based materials such as carbon black, graphene, carbon nanotubes, and carbon nanofiber (CNFs) must be studied owing to their lower cost and stability over time [22–25]. Among them, CNFs are one of the promising reliable candidates because their high surface area (462 m² g^{−1}), low cost, superb electrical conductivity (10² S cm^{−1}), and excellent physical and chemical stability, together with efficient electron transport resulting from their one-dimensional (1–D) nanostructure [26–28]. In addition, the

* Corresponding author.

E-mail address: hjahn@seoultech.ac.kr (H.-J. Ahn).

development of mesoporous CNFs with high surface areas is a key issue because of the enhanced catalytic active sites resulting from the excellent ORR activity. The increased mesopore volume fraction of catalysts can facilitate a short diffusion route and low-resistance pathways resulting from the increase in the number of accessible ions between the acid electrolyte and catalysts. Therefore, a study on advanced nanostructures consisting of metal- and N-doped mesoporous CNFs will be an important technology for high-performance ORR activity. However, there have been no reports of studies on well-dispersed Fe nanoparticles exposed within N-doped mesoporous CNFs for high-performance ORR activity. In this study, well-dispersed Fe nanoparticles exposed within N-doped mesoporous CNFs were successfully synthesized using electrospinning and H₂-activation, and their structural, morphological, and electrochemical properties, including ORR activity and long-term stability, were investigated.

2. Experimental

2.1. Chemicals

Polyacrylonitrile (PAN, $M_w = 150,000$), iron(II) phthalocyanine (FeC₃₂H₁₆N₈), *N*, *N*-dimethylformamide (DMF), Nafion[®] perfluorinated resin solution, 2-propanol (anhydrous), and perchloric acid (HClO₄, ACS reagent 70%) were purchased from Sigma–Aldrich. All chemicals were used without further purification.

2.2. Synthesis of well-dispersed Fe nanoparticles within N-doped mesoporous carbon nanofibers

Fe nanoparticles within N-doped mesoporous CNFs (hereafter referred to as Fe–NMCNF) were synthesized by electrospinning and H₂-activation. First, in order to synthesize Fe nanoparticles within N-doped CNFs (hereafter referred to as Fe–NCNF), PAN and FeC₃₂H₁₆N₈ were dissolved in DMF with vigorous stirring for 3 h. The electrospinning was conducted at a high voltage of ~13 kV and a feeding rate of 0.03 mL h⁻¹. The distance between the 23-gauge needle and the aluminum foil collector was fixed at 15 cm. The prepared as-spun nanofibers were stabilized at 280 °C for 2 h in air and carbonized at 800 °C for 2 h in N₂ gas (99.999%). In order to obtain Fe–NMCNF, the H₂-activation was carried out using a mixed gas (N₂/H₂ = 90%/10%) at three different temperatures—700, 800, and 900 °C—for 5 h; hereafter, the corresponding products are referred to as Fe–NMCNF–700, Fe–NMCNF–800, and Fe–NMCNF–900. In all, we prepared four different types of electrocatalysts: Fe–NCNF, Fe–NMCNF–700, Fe–NMCNF–800, and Fe–NMCNF–900.

2.3. Characterization

The morphologies and structures were observed by field-emission scanning electron microscopy (FESEM; S-4800, Hitachi, Japan) and transmission electron microscopy (TEM; TECNAI F20, FEI, USA). The latter was conducted at the Gwangju center of Korea Basic Science Institute (KBSI), Korea. The crystal structures and chemical bonding states of the samples were characterized using X-ray diffractometry (XRD; D/Max 2500 V, Rigaku, Japan) with Cu K_α radiation in the 2θ range of 10°–90° at a step size of 0.02° and X-ray photoelectron spectroscopy (XPS; ESCALAB 250, Thermo Scientific, USA) with an Al K_α X-ray source. The specific surface area, total pore volume, average pore size, and pore-size distribution of the samples were calculated from the Brunauer–Emmett–Teller (BET) and BJH (Barrett–Joyner–Halenda) measurements using N₂ adsorption at 77 K. The content of the samples was measured using thermogravimetric analysis (TGA; TGA-50, Shimadzu, Japan) from 200

to 1000 °C at a heating rate of 10 °C min⁻¹ in air.

2.4. Electrochemical characterization

Electrochemical measurements of the samples were obtained by a potentiostat/galvanostat (PGSTAT302N, FRA32M, Metrohm Autolab B.V., The Netherlands) in a conventional three-electrode system, consisting of glassy carbon (0.0706 cm²) as the working electrode, a Pt wire as the counter electrode, and Ag/AgCl (sat. KCl) as the reference electrode. Each catalyst ink consisting of an electrocatalyst and Nafion (weight ratio: 8:2) in 2-propanol was loaded onto the glassy carbon electrode and dried in an oven at 50 °C for 30 min. The electrolyte was prepared from a 0.1 M HClO₄ solution. Before starting the electrochemical measurements, the electrolyte was purged with Ar or O₂ gas for 1 h, and a continuous gas flow was maintained during the electrochemical measurement for gas saturation in the test cells. To investigate the electrochemical properties, cyclic voltammograms (CVs) were obtained at a scan rate of 50 mV s⁻¹ in the range of -0.2 to 1.0 V in an Ar-saturated electrolyte. The ORR activity was measured from linear sweep voltammograms at various rotational speeds (400, 900, 1,600, and 2500 rpm) in an O₂-saturated electrolyte by sweeping the potential from 0.8 to 0 V at a scan rate of 5 mV s⁻¹. The long-term stability tests were conducted by collecting CVs for up to 2000 cycles in the voltage range of 0.4–0.9 V at a scan rate of 50 mV s⁻¹ in an O₂-saturated electrolyte. After the long-term stability tests, the ORR activity was investigated from 0.8 to 0 V at a scan rate of 5 mV s⁻¹ and a rotational disk speed of 1600 rpm.

3. Results and discussion

Fig. 1 shows a schematic of the steps for the synthesis of idea, well-dispersed Fe nanoparticles exposed within N-doped mesoporous CNFs. As shown in Fig. 1a, the as-spun nanofibers consisting of PAN and FeC₃₂H₁₆N₈ were prepared by electrospinning, which carried out the carbonization using N₂ gas to obtain Fe–NCNF (Fig. 1b). Finally, the well-dispersed Fe–NMCNF was synthesized because of the vacant sites resulting from the agglomeration of Fe nanoparticles as a result H₂-activation, as shown in Fig. 1c.

To further investigate the surface properties of the samples, the specific surface area, total pore volumes, average pore diameters, and pore volume fraction were examined using BET measurements; the results are summarized in Table 1. The specific surface areas of Fe–NCNF, Fe–NMCNF–700, Fe–NMCNF–800, and Fe–NMCNF–900 are ~294.9, 416.8, 467.6, and 468.9 m² g⁻¹, respectively. Moreover, the total pore volumes and average pore sizes were 0.21 cm³ g⁻¹ and 2.9 nm for Fe–NCNF, 0.63 cm³ g⁻¹ and 6.0 nm for Fe–NMCNF–700, 0.88 cm³ g⁻¹ and 7.5 nm for Fe–NMCNF–800, and 0.95 cm³ g⁻¹ and 8.1 nm for Fe–NMCNF–900. In particular, the mesopore volume fractions of Fe–NCNF, Fe–NMCNF–700, Fe–NMCNF–800, and Fe–NMCNF–900 were 31.6, 72.2, 79.1, and 82.9%, respectively. As the calcination temperature for H₂-activation was increased, the specific surface area, total pore volumes, average pore diameters, mesopore volume fractions gradually increased accordingly because of the extraction and agglomeration of Fe nanoparticles within the CNFs during the H₂-activation. In particular, the pore size distribution and mesopore volume fraction (pore width: 2–50 nm, IUPAC) are very important properties for the exposure of Fe nanoparticles within CNFs. Fig. 2a shows the pore size distributions and mesopore volumes measured by BJH measurements from the N₂ adsorption, in which the pore sizes were in the range of 2–50 nm. After H₂-activation, the mesopore volume fraction of the samples increased as the calcination temperature was increased, which is consistent with the BET results. The enlarged mesopores of

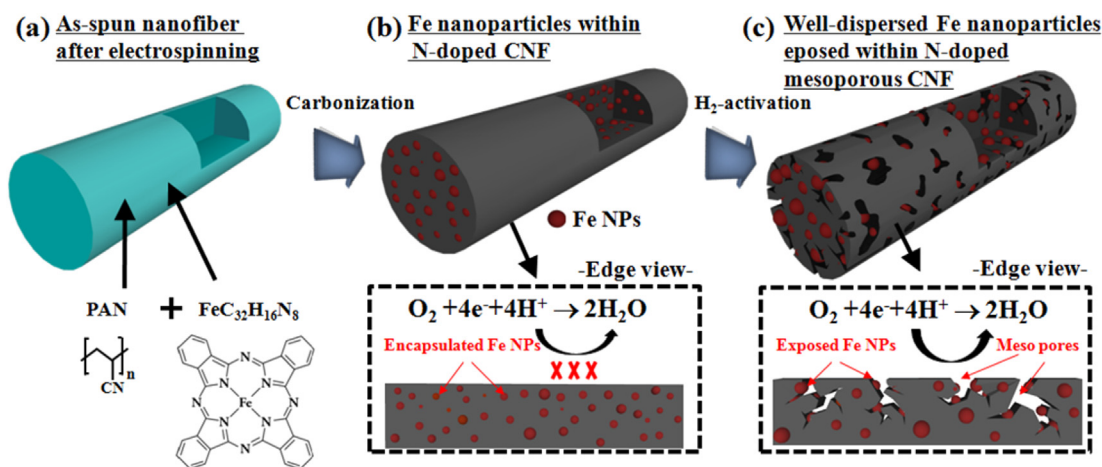


Fig. 1. A schematic of the steps for the synthesis of idea (a) as-spun nanofibers consisting of PAN and $\text{FeC}_{32}\text{H}_{16}\text{N}_8$ using electrospinning (b) Fe–NCNF using carbonization, and (c) well-dispersed Fe–NMCNF using H_2 -activation.

Table 1
BJH pore size distributions and mesopore volumes of the samples.

Samples	S_{BET} [m^2g^{-1}]	Total pore volume ($p/p_0 = 0.990$) [cm^3g^{-1}]	Average pore diameter [nm]	Pore volume fraction	
				V_{micro} (%)	V_{meso} (%)
Fe–NCNF	294.9	0.21	2.9	68.4	31.6
Fe–NMCNF–700	416.8	0.63	6.0	27.8	72.2
Fe–NMCNF–800	467.6	0.88	7.5	20.9	79.1
Fe–NMCNF–900	468.9	0.95	8.1	17.1	82.9

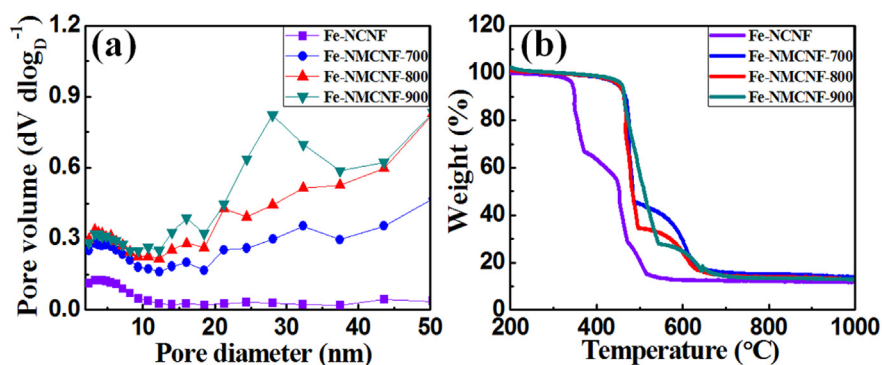


Fig. 2. (a) The BJH pore size distributions of Fe–NCNF, Fe–NMCNF–700, Fe–NMCNF–800, and Fe–NMCNF–900 from the N_2 adsorption (b) TGA curves of Fe–NCNF, Fe–NMCNF–700, Fe–NMCNF–800, and Fe–NMCNF–900 from 200 to 1000 °C at a heating rate of $10\text{ }^\circ\text{C min}^{-1}$ in air.

the samples after H_2 -activation could provide a shorter diffusion route and low resistance pathways between the catalysts and the electrolyte [29–31]. To further examine the content and thermal stability of the samples, TGA analysis was performed from 200 to 1000 °C at a heating rate of $10\text{ }^\circ\text{C min}^{-1}$ in air, as shown in Fig. 2b. All samples exhibited similar weight losses of ~87%, indicating that they had almost the same amount of Fe nanoparticles within the CNFs. In addition, the initial weight loss of Fe–NMCNF–700, Fe–NMCNF–800, and Fe–NMCNF–900 began at approximately 465 °C owing to the relatively high thermal stability, resulting in graphitic growth during the H_2 -activation compared to that of Fe–NCNF.

Fig. 3 shows FESEM images of Fe–NCNF, Fe–NMCNF–700, Fe–NMCNF–800, and Fe–NMCNF–900. All samples had similar average diameters in the range of 293–323 nm. The samples Fe–NCNF (Fig. 2a) and Fe–NMCNF–700 (Fig. 3b) exhibited uniform

morphologies as well as smooth surfaces without any beads resulting from Fe nanoparticles agglomerated on the surface, which implies that the Fe nanoparticles were encapsulated within the CNFs. Fe–NMCNF–800 (Fig. 3c) showed uniform morphology and rough CNF surfaces owing to the porous structures on the CNFs. However, Fe–NMCNF–900 (Fig. 3d) exhibited irregular morphology and rougher CNF surfaces because there were more porous structures and the Fe nanoparticles agglomerated mostly on the surface. In this case, the one-dimensional nanostructures of the prepared CNFs were no longer present. These characteristics would yield poor electrochemical performance in ORR.

Fig. 4 shows the TEM data obtained to examine the morphological and structural properties of the samples. All samples showed relatively dark spots embedded within the CNFs, implying the presence of Fe nanoparticles. The size of the Fe nanoparticles was in the range of 6.1–7.7 nm for Fe–NCNF (Fig. 4a), 10.7–12.1 nm

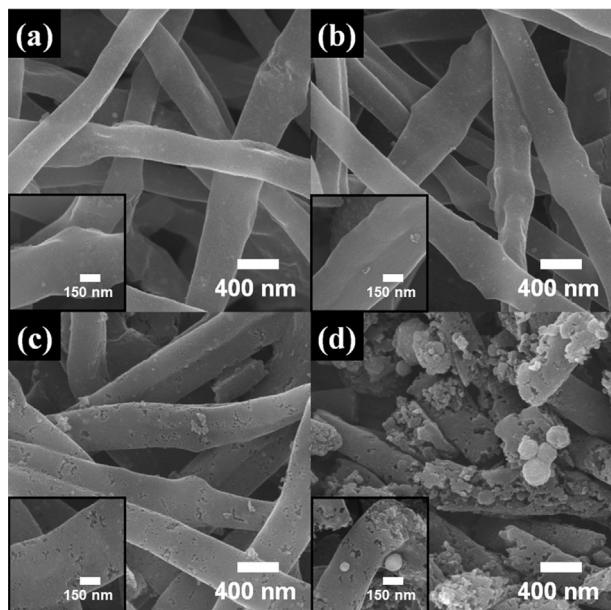


Fig. 3. SEM images and inset SEM images obtained from (a) Fe–NCNF, (b) Fe–NMCNF–700, (c) Fe–NMCNF–800, and (d) Fe–NMCNF–900.

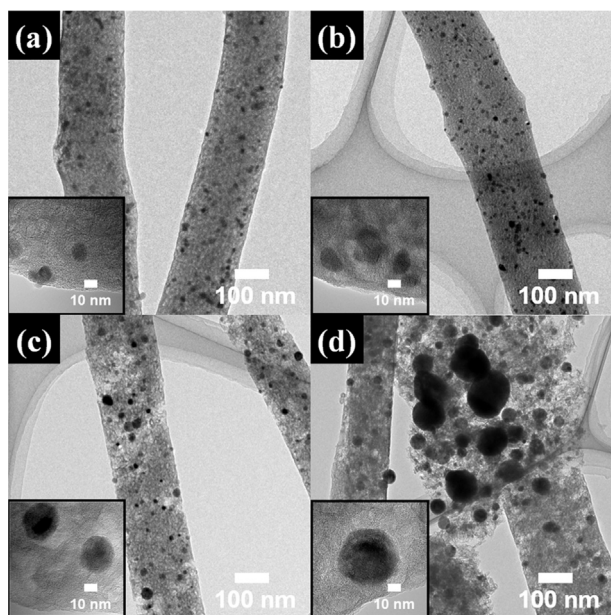


Fig. 4. TEM images and inset TEM images of (a) Fe–NCNF, (b) Fe–NMCNF–700, (c) Fe–NMCNF–800, and (d) Fe–NMCNF–900. High-resolution TEM images of each sample (inset of Fig. 3a–d).

for Fe–NMCNF–700 (Fig. 4b), 17.9–19.3 nm for Fe–NMCNF–800 (Fig. 4c), and 39.1–93.5 nm for Fe–NMCNF–900 (Fig. 4d). The size of Fe nanoparticles increased as the calcination temperature was increased. Interestingly, Fe–NMCNF–800 (Fig. 4c) displayed a unique structure related to the Fe nanoparticles exposed on the NMCNFs as a result of the formation of mesoporous CNFs. However, for Fe–NMCNF–900, the exposed Fe nanoparticles were located within or on the mesoporous CNFs, which exhibited many agglomerated Fe nanoparticles (39.1–93.5 nm) because of the high calcination temperature of 900 °C. Also, Fe–NMCNF–900 was almost collapsed without one-dimensional nanostructures, which

means that the excessive agglomerated Fe nanoparticles could directly break the CNF. The agglomerated Fe nanoparticles could lead to low performance of ORR in an acid electrolyte. Furthermore, the SEM and TEM results indicate that the extraction and agglomeration of Fe nanoparticles in the CNFs during H₂-activation led to the formation of mesoporous structures in the CNFs. In other words, the H₂-activation could provide the extraction and agglomeration of metal phases required to produce more thermodynamically stable phases [32,33]. Accordingly, the Fe nanoparticles were exposed on the CNF edge surface and they could affect the electrochemical performance in ORR because of the increased contact sites between the Fe nanoparticles and the electrolyte.

Fig. 5 shows XRD patterns of the samples obtained to investigate their crystallinities and crystalline phases. All samples exhibited broad peaks at around 25° corresponding to the (002) layers of graphite. The main characteristic diffraction peaks of all samples were observed at 44.7°, 65.0°, and 82.4°, which correspond to the (110), (200), and (211) planes, respectively. These patterns are in good agreement with the Fe phase with a body-centered structure (space group $Im\bar{3}m[229]$; JCPDS card No. 87–0721). Moreover, as the calcination temperature was increased, the full width at half-maximum (FWHM) of the diffraction peaks of the Fe phase became narrow because of the increased size of Fe nanoparticles, which is in good agreement with the FESEM and TEM results.

Fig. 6 shows high-resolution N1s peaks in the XPS spectra of the samples. Typical high-resolution N1s peaks are categorized under four different nitrogen species: pyridinic-N-oxide N (403.0 ± 0.2 eV), graphitic-N (401.0 ± 0.2 eV), pyrrolic-N (400.0 ± 0.2 eV), and pyridinic-N (398.4 ± 0.2 eV) [34,35]. In general, graphitic-N and pyrrolic-N can contribute to possible active sites in ORR [36–38]. Concentration of different nitrogen species of all samples on the surfaces are calculated using fitted XPS curves considering XPS spectra area. As the calcination temperature of H₂-activation was increased, the graphitic-N content was gradually increased from 48.2 wt% (Fe–NCNF) to 55.9 wt% (Fe–NMCNF–700), 61.6 wt% (Fe–NMCNF–800), and 67.3 wt% (Fe–NMCNF–900). Because active H atoms could encourage recrystallization of carbon, including the graphitic growth during H₂-activation [39,40], the increased graphitic-N content may have the improved ORR activity and could have affected the electrochemical performance in ORR. In addition, the pyrrolic-N content of all the samples was observed to have similar values regardless of the calcination temperature. The concentrations of the four different nitrogen species are summarized in Table 2. Thus, N-doped carbon assisted O₂ adsorption and decomposition of intermediate hydroperoxide (HO₂) to oxygen, thereby increasing the catalytic activity in ORR [41].

The ORR activity of the samples was evaluated using CVs in an

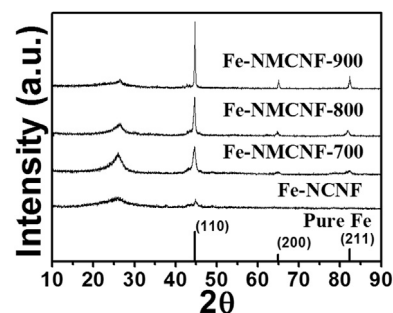


Fig. 5. XRD patterns of Fe–NCNF, Fe–NMCNF–700, Fe–NMCNF–800, and Fe–NMCNF–900 in the 2θ range from 10° to 90°.

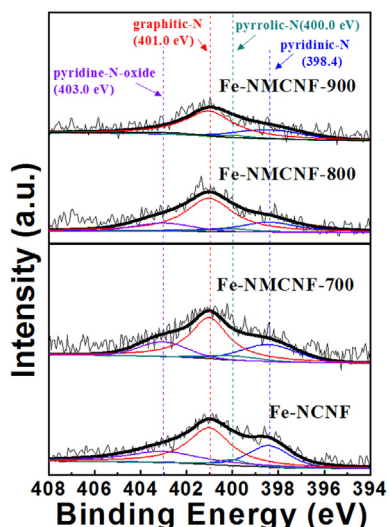


Fig. 6. The N 1s XPS spectra of Fe-NCNF, Fe-NMCNF-700, Fe-NMCNF-800, and Fe-NMCNF-900.

Ar-saturated 0.1 M HClO₄ electrolyte at a scan rate of 50 mV s⁻¹ in the range of -0.2 to 1.0 V, as shown in Fig. 7a. The pairs of well-defined peaks observed at 0.3–0.4 V in the CVs correspond to the Fe(II)/Fe(III) redox reaction [42,43], which was directly related to the high catalytic activity in ORR [44]. Fe-NMCNF-800 exhibited

the broadest capacitive current among the samples, indicating that it had the highest electrochemically accessible area. For Fe-NMCNF-800, the performance improvement in the capacitive current can be explained by the existence of Fe nanoparticles exposed within the mesoporous CNFs during H₂-activation at the optimum calcination temperature of 800 °C.

To further investigate the ORR activity of the samples, the linear scanning voltammetry (LSV) measurements were obtained using a rotating disk electrode (RDE) with a speed of 1600 rpm in an O₂-saturated 0.1 M HClO₄ electrolyte, as shown in Fig. 7b. For comparison, similar LSV measurements were also obtained for the commercial Pt/C catalyst (40 wt% Pt on Vulcan carbon, E-TEK, now division of Industriel De Nora S.P.A., Italy). All prepared samples shown in Fig. 7b exhibited noticeable ORR activities. However, the conventional CNF without N-doping showed a poor electrocatalytic activity, indicating that the introduction of N-doping in CNF can strikingly provide ORR activities. In particular, the ORR onset potential can demonstrate the electrocatalytic activity of the catalysts. The onset potentials of commercial Pt/C, Fe-NCNF, Fe-NMCNF-700, Fe-NMCNF-800, and Fe-NMCNF-900 were approximately 0.63, 0.52, 0.53, 0.59, and 0.56 V, respectively, which means that the optimum calcination temperature during H₂-activation was 800 °C. In addition, a half-wave potential ($E_{1/2}$) of 0.51 V was observed for Fe-NMCNF-800, which shows a gap of only 13 mV when compared to $E_{1/2}$ of the commercial Pt/C. Moreover, the kinetic limiting current density at 0.51 V (2.1 mA cm⁻²) was close to that of the commercial Pt/C catalyst (2.6 mA cm⁻²). The improved electrocatalytic activity of Fe-NMCNF-800 may be

Table 2
Concentration of different nitrogen species of the samples on the surfaces.

Samples	Concentration of different nitrogen species (%)			
	Pyridinic (398.4 eV ± 0.3 eV)	Pyrrolic (400.0 eV ± 0.3 eV)	Graphitic (401.0 eV ± 0.3 eV)	Pyridine (403.0 eV ± 0.3 eV)
Fe-NCNF	21.2	4.6	48.2	26
Fe-NMCNF-700	22.3	5.1	55.9	16.7
Fe-NMCNF-800	21.8	4.5	61.6	12.1
Fe-NMCNF-900	22.2	5	67.3	5.5

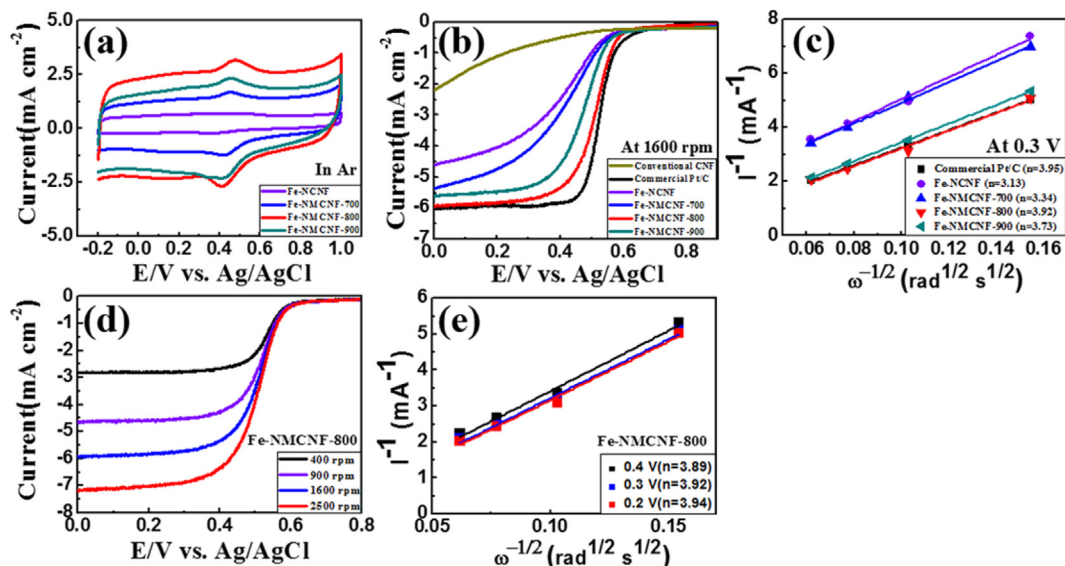


Fig. 7. (a) CV curves of samples in an Ar-saturated 0.1 M HClO₄ electrolyte at a scan rate of 50 mV s⁻¹ in the range of -0.2 to 1.0 V, (b) The polarization curves of commercial Pt/C, Fe-NCNF, Fe-NMCNF-700, Fe-NMCNF-800, and Fe-NMCNF-900 in an O₂-saturated 0.1 M HClO₄ electrolyte at a sweep rate of 5 mV s⁻¹ at rotational speeds of 1600 rpm. (c) Koutecky–Levich plots of commercial Pt/C, Fe-NCNF, Fe-NMCNF-700, Fe-NMCNF-800, and Fe-NMCNF-900 at 0.3 V. (d) The polarization curves of Fe-NMCNF 800 in an O₂-saturated 0.1 M HClO₄ electrolyte at a sweep rate of 5 mV s⁻¹ at various rotational speeds in range from 400, 900, 1,600, and 2,500 rpm. (e) Koutecky–Levich plots of Fe-NMCNF-800 at potentials of 0.2, 0.3, and 0.4 V.

attributed to the enhanced active sites resulting from the Fe nanoparticles exposed within the mesoporous CNFs and the increased graphitic-N content.

To examine the ORR kinetic process, the number of electron transfer (n) was analyzed using the Koutecky–Levich (K–L) equation [18,45]:

$$\frac{1}{j} = \frac{1}{j_k} + \frac{1}{j_d} = \frac{1}{nFkC_{O_2}^b} + \frac{1}{0.62nFD_{O_2}^{2/3}v^{-1/6}C_{O_2}^b\omega^{1/2}}$$

where j is the measured current density, j_k is current density in the kinetic part, j_d is current density in the diffusion part, n is the number of electrons transferred during a ORR process, F is the Faraday constant ($F = 96,485 \text{ C mol}^{-1}$), k is the electron transfer rate constant, C_{O_2} is the bulk concentration ($C = 1.26 \times 10^{-3} \text{ mol L}^{-1}$), D_{O_2} is the diffusion coefficient in the 0.1 M HClO₄ electrolyte ($D = 1.93 \times 10^{-5} \text{ cm}^2 \text{ s}^{-1}$), v is the kinetic viscosity of the electrolyte ($v = 1.009 \times 10^{-2} \text{ cm}^2 \text{ s}^{-1}$), and ω is the angular velocity of the disk ($\omega = 2\pi N$, N is the linear rotational rate) [18,45]. Fig. 7c shows the Koutecky–Levich (K–L) plots for all samples calculated at 0.3 V. The n value of all samples was calculated to be 3.95 for the commercial Pt/C catalyst, 3.13 for Fe–NCNF, 3.34 for Fe–NMCNF–700, 3.92 for Fe–NMCNF–800, and 3.73 for Fe–NMCNF–900. The high n values of the commercial Pt/C and Fe–NMCNF–800 imply that they had nearly four-electron pathways in an acid electrolyte. Fig. 7d shows the polarization curves of Fe–NMCNF–800 at different rotational speeds (400–1600 rpm). All the curves display well-defined diffusion-limiting currents. The ORR current density of the sample increased as the rotation rate was increased, which can be ascribed to the fast oxygen diffusion at high speeds. Fig. 7e shows the K–L plots of Fe–NMCNF–800 calculated at different potentials of 0.2, 0.3, and 0.4 V. These plots show good linearity and parallelism, which imply that the sample had first-order kinetics with respect to the convergence of oxygen [46,47]. The n values of Fe–NMCNF–800 calculated at 0.2, 0.3, and 0.4 V were 3.89, 3.92, and 3.94, respectively. Thus, it is noted that Fe–NMCNF–800 with nearly four-electron pathways exhibited superb ORR activity in a wide voltage window.

Furthermore, one of the important criteria for catalysts is long-term stability in ORR. In our study, the long-term stability of all samples was evaluated using cycling between 0.4 and 0.9 V for 2000 cycles at a scan rate of 50 mV s^{-1} in an O₂-saturated electrolyte, as shown in Fig. 8a–e. Potential degradations in $E_{1/2}$ were observed at 46 mV for the commercial Pt/C catalyst, 90 mV for Fe–NCNF, 36 mV for Fe–NMCNF–700, and 58 mV for Fe–NMCNF–900. In particular, Fe–NMCNF–800 displayed the lowest potential degradation in $E_{1/2}$, which indicates its excellent long-term stability in ORR. Fig. 8f shows the kinetic current density of all samples calculated at 0.5 V before and after 2000 cycles. Before the cycling tests, the commercial Pt/C catalyst showed a kinetic current density of 4.42 mA cm^{-2} , which was higher than that of Fe–NMCNF–800 (3.41 mA cm^{-2}). However, after 2000 cycles, the kinetic current density of Fe–NMCNF–800 (2.67 mA cm^{-2}) with excellent kinetic current density retention of 78.3% was slightly higher than that of the commercial Pt/C catalyst (2.63 mA cm^{-2}) with poor kinetic current density retention of 59.5%. In other words, among all the samples, Fe–NMCNF–800 exhibited the best long-term stability in ORR. However, after 2000 cycles, Fe–NMCNF–900 exhibited a low kinetic current density of 0.86 mA cm^{-2} with poor kinetic current density retention of 46.5% owing to the formation of agglomerated Fe nanoparticles and the destruction of mesoporous CNFs. Therefore, the performance improvement (including ORR activity and long-term stability) of Fe–NMCNF–800 can be explained by two main effects: well-dispersed Fe nanoparticles exposed within N-doped CNFs; the uniform morphology of mesoporous CNFs was preserved. As a result, Fe–NMCNF–800 can be utilized as a promising catalyst for cathodes in PEMFCs and metal-air batteries.

4. Conclusions

Well-dispersed Fe nanoparticles within N-doped mesoporous carbon nanofibers, Fe–NMCNF–800, with enhanced mesopore volume fraction were synthesized using electrospinning and H₂-activation. Fe–NMCNF–800 exhibited a high specific surface area of $467.6 \text{ m}^2 \text{ g}^{-1}$, total pore volume of $0.88 \text{ cm}^3 \text{ g}^{-1}$, large average

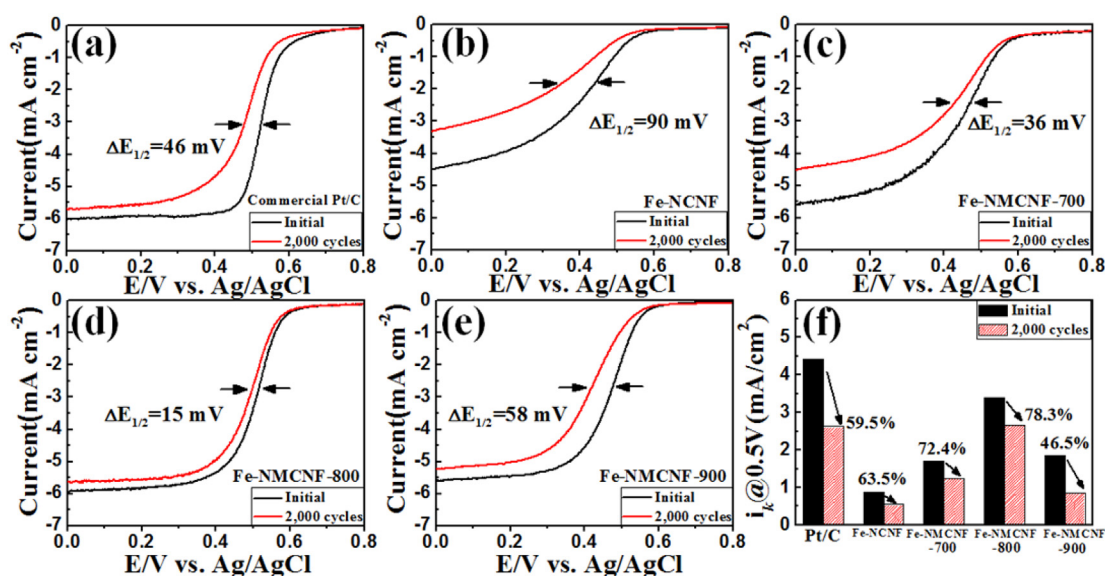


Fig. 8. Polarization curves of (a) commercial Pt/C, (b) Fe–NCNF, (c) Fe–NMCNF–700, (d) Fe–NMCNF–800, and (e) Fe–NMCNF–900 before and after long-term stability test in an O₂-saturated 0.1 M HClO₄ electrolyte at a scan rate of 5 mV s^{-1} at rotational speeds of 1600 rpm. The long-term stability tests were conducted using CVs up to 2000 cycles in the range of 0.4–0.9 V at a scan rate of 50 mV s^{-1} in an O₂-saturated electrolyte. (f) Comparison of kinetic current density of commercial Pt/C, Fe–NCNF, Fe–NMCNF–700, Fe–NMCNF–800, and Fe–NMCNF–900 at 0.5 V before and after 2000 cycles.

pore size of 7.5 nm, large mesopore volume fraction of 79.1%, and increased graphitic-N content of 61.6%. Fe–NMCNF–800 showed excellent ORR activity such as onset potential of 0.59 V, half-wave potential ($E_{1/2}$) of 0.51 V, kinetic limiting current density of 2.1 mA cm⁻² (at 0.51 V), and four-electron reduction pathways ($n = 3.92$); these values are almost similar to those of the commercial Pt/C catalyst. Furthermore, the superb long-term stability of Fe–NMCNF–800 after 2000 cycles resulted in lower potential degradation of 15 mV in $E_{1/2}$, higher kinetic current density of 2.67 mA cm⁻², and superior kinetic current density retention of 78.3% when compared to the commercial Pt/C catalyst. Thus, the superb electrochemical performance is attributed to the well-dispersed Fe nanoparticles exposed within N-doped mesoporous CNFs and the uniform morphology of the mesoporous CNFs.

Acknowledgments

This work was supported by the International Collaborative Energy Technology R&D Program of the Korea Institute of Energy Technology Evaluation and Planning (KETEP), granted financial resource from the Ministry of Trade, Industry & Energy, Republic of Korea. (No. 20138520030800).

References

- [1] J. Snyder, T. Fujita, M.W. Chen, J. Erlebacher, *Nat. Mater.* 9 (2010) 904–907.
- [2] K. Huang, Q.N. Ling, C.H. Huang, K. Bi, W.J. Wang, T.Z. Yang, Y.K. Lu, J. Liu, R. Zhang, D.Y. Fan, Y.G. Wang, M. Le, *J. Alloys Compd.* 646 (2015) 837–842.
- [3] M.K. Jeon, C.H. Lee, G.I. Park, K.H. Kang, *J. Power Sources* 216 (2012) 400–408.
- [4] G. Wang, H. Wu, D. Wexler, H. Liu, O. Savadogo, *J. Alloys Compd.* 503 (2010) L1–L4.
- [5] M. Lefèvre, E. Proietti, F. Jaouen, J.–P. Dodelet, *Science* 324 (2009) 71–74.
- [6] K. Gong, F. Du, Z. Xia, M. Durstock, L. Dai, *Science* 323 (2009) 760–764.
- [7] K. Yamamoto, T. Imaoka, W.–J. Chun, O. Enoki, H. Katoh, M. Takenaga, A. Sonoi, *Nat. Chem.* 1 (2009) 397–402.
- [8] Z. Yang, H. Nie, X. Chen, X. Chen, S. Huang, *J. Power Sources* 236 (2013) 238–249.
- [9] A. Ezeta, E.M. Arce, O. Solorza, R.G. González, H. Dorantes, *J. Alloys Compd.* 483 (2009) 429–431.
- [10] D. Banham, S. Ye, K. Pei, J. Ozaki, T. Kishimoto, Y. Imashiro, *J. Power Sources* 285 (2015) 334–348.
- [11] R. Jasinski, *Nature* 201 (1964) 1212–1213.
- [12] S.–H. Liu, J.–R. Wu, *Electrochim. Acta* 135 (2014) 147–153.
- [13] J. Yin, Y. Qiu, J. Yu, *Electrochem. Solid–State Lett.* 2 (2013) M37–M39.
- [14] J. Yin, Y. Qiu, J. Yu, *Electrochem. Commun.* 30 (2013) 1–4.
- [15] C. Domínguez, F.J.P. Alonso, J.L.G. Fuente, S.A.A. Thabaiti, S.N. Basahel, A.O. Alyoubi, A.A. Alshehri, M.A. Pena, S. Rojas, *J. Power Sources* 271 (2014) 87–96.
- [16] S.–H. Liu, J.–R. Wu, C.–J. Pan, B.–J. Hwang, *J. Power Sources* 250 (2014) 279–285.
- [17] Z. Wen, S. Ci, F. Zhang, X. Feng, S. Cui, S. Mao, S. Luo, Z. He, J. Chen, *Adv. Mater.* 24 (2012) 1399–1404.
- [18] H. Peng, Z. Mo, S. Liao, H. Liang, L. Yang, F. Luo, H. Song, Y. Zhong, B. Zhang, *Sci. Rep.* 3 (2013) 1765.
- [19] Y.–L. Liu, X.–Y. Xu, P.–C. Sun, T.–H. Chen, *Int. J. Hydrogen Energy* 40 (2015) 4531–4539.
- [20] Y. Hu, J.O. Jensen, W. Zhang, L.N. Cleemann, W. Xing, N.J. Bjerrum, Q. Li, *Angew. Chem. Int. Ed.* 53 (2014) 1765.
- [21] Y. Nie, L. Li, Z. Wei, *Chem. Soc. Rev.* 44 (2015) 2168–2201.
- [22] M. Liu, R. Zhang, W. Chen, *Chem. Rev.* 114 (2014) 5117–5160.
- [23] G. Wu, P. Zelenay, *Acc. Chem. Res.* 46 (2013) 1878–1889.
- [24] K.B. Liew, W.R.W. Daud, M. Ghasemi, J.X. Leong, S.S. Lim, M. Ismail, *Int. J. Hydrogen Energy* 39 (2014) 4870–4883.
- [25] C.W.B. Bezerra, L. Zhang, K. Lee, H. Liu, A.L.B. Marques, E.P. Marques, H. Wang, J. Zhang, *Electrochim. Acta* 53 (2008) 4937–4951.
- [26] G.–H. An, H.–J. Ahn, *J. Power Sources* 272 (2014) 828–836.
- [27] G.–H. An, H.–J. Ahn, W.–K. Hong, *J. Power Sources* 274 (2015) 536–541.
- [28] G.–H. An, H.–J. Ahn, *J. Electroanal. Chem.* 744 (2015) 32–36.
- [29] X. Bo, Y. Zhang, M. Li, A. Nsabimana, L. Guo, *J. Power Sources* 288 (2015) 1–8.
- [30] H. Huang, Q. Wang, Q. Wei, Y. Huang, *Int. J. Hydrogen Energy* 40 (2015) 6072–6084.
- [31] B.–H. Kim, K.S. Yang, J.P. Ferraris, *Electrochim. Acta* 75 (2012) 325–331.
- [32] D.–H. Nam, J.–H. Lee, N.–R. Kim, Y.–Y. Lee, H.–W. Yeon, S.–Y. Lee, Y.–C. Joo, *Carbon* 82 (2015) 273–281.
- [33] G.–H. An, H.–J. Ahn, *Carbon* 65 (2013) 87–96.
- [34] Y.–L. Liu, X.–Y. Xu, P.–C. Sun, T.–H. Chen, *Int. J. Hydrogen Energy* 40 (2015) 4531–4539.
- [35] J. Wang, G. Wang, S. Miao, Xiaole Jiang, Jiayuan Li, Xinhe Bao, *Carbon* 75 (2014) 381–389.
- [36] E. Negro, A.H.A.M. Videla, V. Baglio, A.S. Aricò, S. Specchia, G.J.M. Koper, *Appl. Catal. B Environ.* 166–167 (2015) 75–83.
- [37] S. Yasuda, L. Yu, J. Kima, K. Murakoshi, *Chem. Commun.* 49 (2013) 9627–9629.
- [38] J. Zhang, D. He, H. Su, X. Chen, M. Pan, S. Mu, *J. Mater. Chem. A* 2 (2014) 1242–1246.
- [39] X. Pan, X. Bao, *Chem. Commun.* (2008) 6271–6281.
- [40] Y. Qiu, J. Yin, H. Hou, J. Yu, X. Zuo, *Electrochim. Acta* 96 (2013) 225–229.
- [41] S. Maldonado, K.J. Stevenson, *J. Phys. Chem. B* 109 (2005) 4707–4716.
- [42] F.J.P. Alonso, M.A. Salam, T. Herranz, J.L.G. Fuente, S.A.A. Thabaiti, S.N. Basahel, M.A. Peña, J.L.G. Fierro, S. Rojas, *J. Power Sources* 240 (2013) 494–502.
- [43] H. Xiao, Z.–G. Shao, G. Zhang, Y. Gao, W. Lu, B. Yi, *Carbon* 57 (2013) 443–451.
- [44] K. Parvez, S. Yang, Y. Hernandez, A. Winter, A. Turchanin, X. Feng, K. Mullen, *ACS Nano* 6 (2012) 9541–9550.
- [45] N. Alexeyeva, E. Shulga, V. Kisand, I. Kink, K. Tammeveski, *J. Electroanal. Chem.* 648 (2010) 169–175.
- [46] J. Yin, Y. Qiu, J. Yu, *J. Electroanal. Chem.* 702 (2013) 56–59.
- [47] R. Liu, D. Wu, X. Feng, K. Mullen, *Angew. Chem. Int. Ed.* 49 (2010) 2565–2569.